See the Darkest Regions of the Moon with Synthetic Aperture Radar and CycleGAN

Tong Xia, Niutao Liu*, Member, IEEE, Yi Zheng, Ya-Qiu Jin, Life Fellow, IEEE, and Feng Xu, Senior Member, IEEE

***Abstract*—There are permanent shadow regions (PSR) where no direct solar illumination is available at lunar poles due to a rotation tilt angle of 1.54°. Few studies about PSR are conducted because the optical images are scarce. Due to the large incidence angle of the scattered light and the shadow of terrain, ShadowCam onboard Korea Pathfinder Lunar Orbiter satellite cannot capture the morphological features within secondary shadow region (SSR) and the distribution of rocks, which hinder the study of PSR. Synthetic Aperture Radar (SAR) can acquire the image of PSR without solar illumination and is sensitive to the rocks with size of meters. But the usage of SAR image is limited by low resolution and difficulty in interpretation. In this paper, SRGAN and CycleGAN are utilized to produce high-resolution optical images of PSR with a resolution of 1.9 m/pixel. The SAR illumination direction is interpreted as the lighting direction. The generated optical images reveal the distribution of rocks within the PSR and the morphology of the darkest SSR, which was never seen before. This method can be used to search for lava tubes within the PSR, where volatile substances from volcanic activity may be preserved.**

***Index Terms*—the darkest regions of the Moon, PSR, SAR, CycleGAN, Mini-RF, Crater, ejecta blanket**

I. Introduction

THE Moon's axial tilt is 1.54°[1]. There is no direct solar illumination in some craters near the lunar poles all the year. These areas are referred to as Permanently Shadowed Regions (PSR)[2]. PSR is attaching global attention but researches about PSR are limited due to the lack of optical images[3]. Questions regarding whether the internal morphology of PSR is unique and how to judge the degree of degradation of craters in PSR, which still need to be addressed.

The scattered sunlight by nearby elevated terrain is the main lighting source in PSR[2]. The Narrow Angle Camera (NAC) of Lunar Reconnaissance Orbiter Cameras (LROC) has imaged the interiors of all PSRs which are larger than 20 km², with long-time exposure techniques[4]. The resolution ranges from 10 to 20 m/pixel. The advanced ShadowCam imager onboard the Korea Pathfinder Lunar Orbiter, which is specifically designed for PSR imaging[5], acquired optical images with resolution of 1.7 m/pixel. However, images are affected by shadows of the scattered light, which made some secondary shadow regions (SSR) still unobservable[6]. Additionally, ShadowCam images are not sensitive to rocks with size of meters due to large incidence angle of the scattered light. Therefore, these images cannot be used to determine the degree of degradation of craters within the PSR[6].

Impact events, such as meteorite collisions with the lunar surface or volcanic eruptions, can cause the ejection and scattering of rocks. Large boulders are often found around lava tubes and fresh craters. The presence of rocks will influence lander path planning. In addition, the degree of degradation of these rocks plays a significant role in understanding the evolution of lunar terrain and inferring the age of specific regions. Previous studies have focused solely on high-resolution LROC NAC optical images in low-latitude regions, lacking research on rocks in PSR. Moreover, rocks in PSR are difficult to be detected by using other remote sensing data sources, such as Digital Elevation Model (DEM)[6].

Synthetic Aperture Radar (SAR) actively emits electromagnetic waves to detect the topography of the lunar poles and does not rely on external light sources[7]. The hybrid-polarized SAR miniature radio frequency (Mini-RF) is designed to detect the PSR of the Moon. Since the wavelength of microwave is much longer than that of visible light, SAR is sensitive to rocky areas, roughness, and undulations that are larger than the wavelength. The disadvantages of the current SAR images are the low resolution and the influence of speckle noise, leading to the difficulty in interpretation[8-11].

Artificial intelligence (AI) proves to be a powerful tool for SAR image interpretation. To enhance the interpretability of SAR image, Generative Adversarial Network (GAN) can transform SAR images into optical images that align better with human visual perception[12], while traditional computer vision methods can hardly describe the nonlinear relationships between SAR and optical images. In this paper, Real Super-Resolution GAN (RealSRGAN) super-resolution technology is adopted to further enhance the resolution of SAR images by 4 times[13]. By utilizing the CycleGAN network, it facilitates the transformation of SAR images into optical images[14]. The generated optical images with RealSRGAN and CycleGAN are free from speckle noise and are easy to understand. With the generated optical images, some fresh craters with ejecta blanket

Manuscript received …… This work was supported in part by the National Natural Science Foundation of China under Grant 62495032 and Grant 62201154, and in part the Chenguang Program of Shanghai Education Development Foundation and Shanghai Municipal Education Commission.

Tong Xia, Niutao Liu, Yi Zheng, Ya-Qiu Jin and Feng Xu are with the Key Laboratory of Information Science of Electromagnetic Waves (MoE), Fudan University, Shanghai 200433, China (corresponding e-mail to Niutao Liu: ntliu@fudan.edu.cn).

Digital Object Identifier….

in PSR are identified. The detailed morphology of SSR is presented.

II. Method And Data

A) Method

RealSRGAN is designed to produce high-resolution images from low-resolution SAR images with enhanced details[13]. RealSRGAN not only focuses on restoring image details but also takes into account the realism and visual quality of the generated images. The network employs adversarial training, combining the structures of a generator and a discriminator. The generator is responsible for mapping low-resolution images to high-resolution images, while the discriminator evaluates the authenticity of the generated images[15]. RealSRGAN employs multiple loss functions, including perceptual loss and adversarial loss, to ensure that the generated images have a higher degree of visual realism[13].

CycleGAN can perform image-to-image translation without a paired training data set. CycleGAN uses cycle consistency loss to ensure that the transformations are coherent and meaningful. CycleGAN trains two generator networks: one maps images from domain one to domain two, while the other performs the reverse mapping. The cycle consistency loss ensures that when an image is transformed to another domain and then back to the original domain, the generated images in original domain one remain unchanged.

B) Data

In this study, NAC data, ShadowCam data, and Mini-RF data were used, with resolutions of 2 m/pixel, 1.7 m/pixel, and 7.5 m/pixel, respectively.

ShadowCam has an instantaneous field of view of 17 micro-radians and a swath width of 2.86° (3072 pixels). The internal memory buffer limits the down-track dimension to 84,992 lines[5].

Mini-RF onboard Lunar Reconnaissance Orbiter (LRO) transmits circular polarization and receives linear polarization with an incidence angle of about 49°[7]. The first Stokes parameter products present the total backscattering from lunar surface. This paper utilizes the first Stokes product from Mini-RF with a spatial resolution of 7.5 m/pixel at S band.

During training, large SAR images are segmented into small images with size of 2048×2048 pixels. High-resolution LRO NAC optical images of low-latitude maria and highlands with a resolution of 2 m/pixel are also segmented into small images with size of 6900×6900 pixels. The lengths of the SAR images and optical images are the same. But the SAR images and the optical images do not need to be registered.

III. Results

A) Validation

Before generating optical images, super-resolution SAR images are produced with RealSRGAN. Fig. 1 presents the original SAR image and the super-resolution SAR image of a fresh crater at the lunar south pole. The crater locates at (84.02°S, 172.00°E). The resolution of the original SAR image is 7.5 m/pixel and the resolution of the super-resolution SAR image is 1.9 m/pixel. In the super-resolution SAR image, the edges of small craters and ejecta blanket become smoother, attributed to the enhanced resolution. It is easier to identify rocks and small craters with several pixels in the super-resolution SAR image.

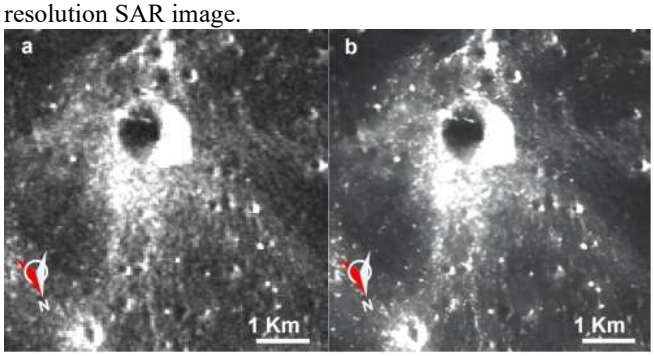

Fig.1. Super-resolution result of SAR images. a, SAR image of a crater from the lunar south pole, with a resolution of 7.5 m/pixel, centered at coordinates (84.02°S, 172.00°E). b, SAR image after 4x super-resolution, achieving a resolution of 1.9 m/pixel.

The optical images are generated with the super-resolution SAR images. To validate the generated optical images, some typical lunar morphologies are selected. Fig. 2 presents the LROC optical images, SAR images, and generated optical images of shaded crater wall of pan-like crater, bowl-like crater, undulated topography with craters, and flat regions. The selected regions locate at (83.96°S, 145.51°E), (84.49°S, 163.48°E), (82.54°S, 150.32°E), and (80.74°S, 148.61°E).

The first column in Fig. 2 contains optical images from the LROC NAC, with a resolution of 2 m/pixel. The second column is SAR images and the third column in Fig. 2 is the generated optical images with resolution of 1.9 m/pixel. The generated optical images effectively restore both large-scale features, such as crater wall of large craters, undulating topography, flat region, and midsize craters, and small-scale lunar surface morphology, including small craters, folds, textures of large crater walls, and ejecta blanket.

In the generated optical images, the illumination direction is the same as the observation direction of the SAR. In generated optical images in Figs. 2c, f, i, and l, slopes facing the radar appear brighter while slopes facing away from the radar are darker. The characteristic is consistent with the true optical image, where slopes facing the Sun are bright and slopes facing away from the Sun are dark. In addition, the ejecta blankets with large amount of rocks are bright in generated images in Fig. 2c, which is the same as the true optical image with small solar illumination angles. For true optical images with large solar illumination angles at high latitude in Fig. 2a, rocks with meter size are difficult to be identified.

To better restore the topographical features in the generated optical images, this study trained highland and Mare models based on the characteristics of lunar topography. For highland, which is bright in optical images, most areas are with significant topographical variation. At Mare, the terrain is relatively flat at most regions and is dark in optical images. The images of

undulating regions are generated with the highland model, allowing the optical images to restore the topographical variations. For relatively flat terrain, the Mare model is employed.

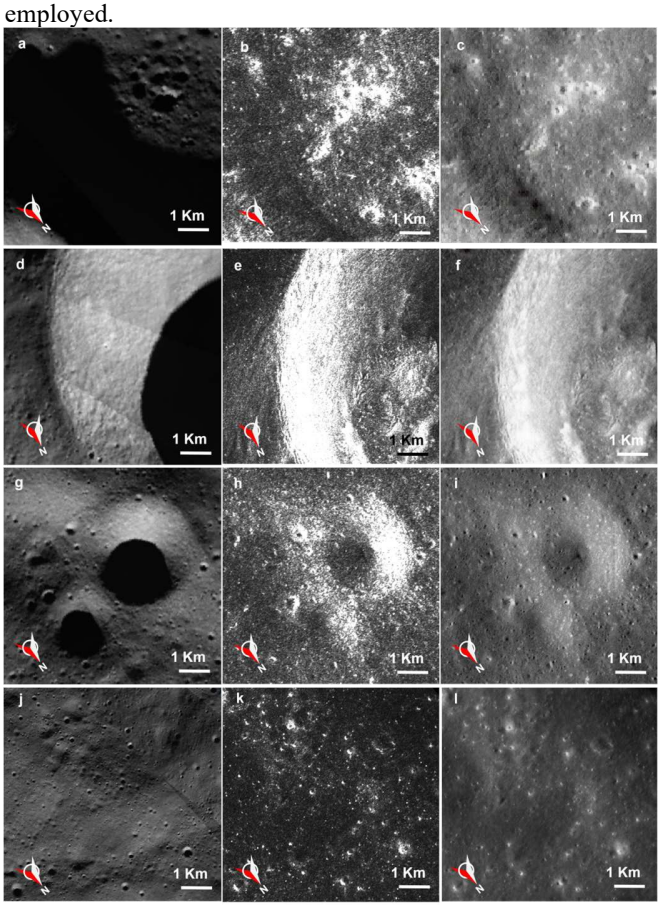

Fig. 2. A Validation of the Images Generated from the PSR. a-c, Pan-like crater, with the central position at (83.96°S, 145.51°E). d-f, Bowl-like crater, with the central position at (83.96°S, 145.51°E). g-i, Undulated topography with craters, with the central position at (83.96°S, 145.51°E). j-l, Flat region, with the central position at (83.96°S, 145.51°E). First Column: Optical images captured by the LROC NAC, with a resolution of 2.0 m/pixel. Due to the angle of sunlight and the crater walls, these images exhibit significant shadowing. Second Column: The SAR images generated from Mini-RF data, with a resolution of 7.5 m/pixel. The echo strength is strong in radar-facing areas and weak in areas facing away from the radar. Similarly, rocky regions show strong echoes while flat areas show weaker echoes. Third Column: The generated optical images with a resolution of 1.9 m/pixel, which reduce shadowing and are sensitive to rocky areas.

Although the resolution can reach 1.9 m/pixel, some small craters may be missed in the generated optical image compared with the true optical image because the resolution of the original SAR image is limited.

B) Secondary Shadow Region

PSR optical images can be captured by using long-time exposure cameras. SSR is the regions in PSR where first-order scattered light cannot reach. SSRs usually appear in craters within the PSR. Due to the large incidence angle of scattered light (greater than 70°) in PSR[2], some regions in craters within PSR can not receive the first-order scattered light. ShadowCam and LROC can not observe most of SSR.

Due to the lack of sunlight in secondary craters, the temperatures within SSR are lower than those in PSR. SSR are suitable for the preservation of volatile substances. Obtaining optical images of SSR is crucial for understanding their morphological characteristics.

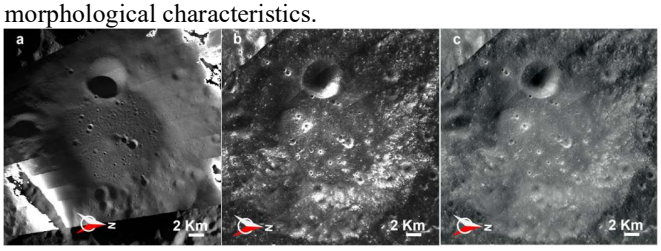

Fig. 3. Images of Faustini Crater in PSR. a, The optical image is from ShadowCam. The ShadowCam images are M028416301S, M028430443S, M02844585S, M028458726S, and M028472867S. The center coordinates of Faustini Crater are (87.18°S, 84.31°E), and the crater floor lies within a PSR. Above the crater, there is a large SSR. b, SAR image of the Faustini Cater. c, The generated optical image can observe the SSR.

The Faustini Crater in Fig. 3 locates at (87.18°S, 84.31°E) at the lunar south polar. Fig. 3a is the optical image from ShadowCam. Because the illumination source of PSR is mainly from the scattered light from the directly illuminated crater wall, the incidence angle of the scattered light in PSR are greater than 70°[2]. Therefore, the optical image from ShadowCam is consistent in style with the no-PSR optical images taken at high solar incidence angles, which are dark and can not distinguish the rocky ejecta blanket. In contrast, the rocky ejecta blankets are bright in the generated image in Fig. 3c.

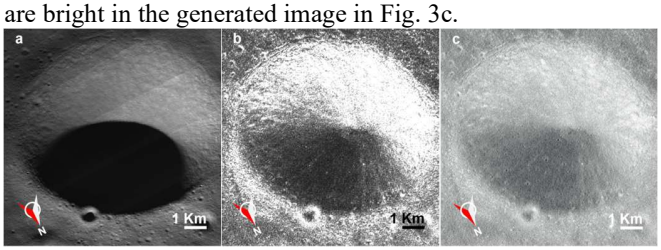

Fig. 4. Images of the largest secondary crater in the Faustini Crater. a, The optical image is from ShadowCam, which shows the presence of SSR. b, The SAR image with a resolution of 7.5 m/pixel. c, The generated optical image reveals the morphology of the crater.

Fig. 4 shows a SSR at (87.23°S, 75.84°E) in the PSR of Faustini Crater. This crater is a bowl-shaped crater with a diameter of 8.3 km. Fig. 4a is the image from ShadowCam. The shadowed region is invisible. Figs. 4b and c present the SAR image and the generated optical image. The small craters and textures of the crater wall of the shaded side in ShadowCam image are visible in the generated image. This crater has no ejecta blanket outsize. The bright regions on the crater wall are rockfall in the generated optical image. This crater is a moderately degraded crater.

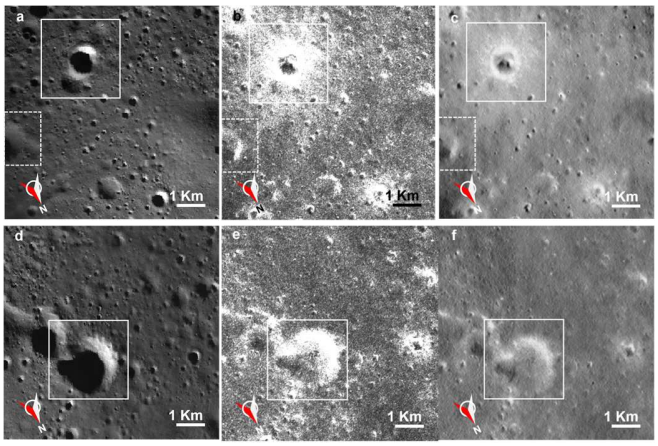

Fig. 5. Images of secondary craters in the Faustini crater. a-f, These secondary craters in Faustini Crater are located at (87.35°S, 84.00°E) and (87.12°S, 85.28° E), respectively. a, d, The Optical images from ShadowCam exist the SSR. b, e, The corresponding SAR images, with a resolution of 7.5 m/pixel, show information about the crater bottoms and surrounding pixel-level craters. c, f, The generated optical images retain all information from the SAR images and reveal details about the crater bottoms of the secondary craters.

Figs. 5a and d are enlarged optical images in Fig. 3. In Fig. 5, the bottoms of some small craters remain in shadow. Figs. 5b and e are the original SAR images with a resolution of 7.5 m/pixel. Figs. 5c and f are the generated optical images with a higher resolution of 1.9 m/pixel. In these images, shadows are removed. The topographic depressions located in the white dashed box in Fig. 5 are distinctly restored in Fig. 5c. The generated optical images align with those captured at low latitudes and small solar incidence angles. They retain the advantages of SAR images in detecting undulations and ejecta blanket. Rocky ejecta blankets within PSR in Fig. 5a cannot be observed by ShadowCam. Because optical images with solar incidence angles greater than 70° are insensitive to lunar surface rocks[2].

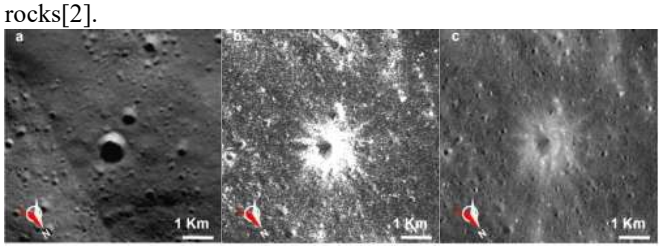

Fig. 6. Optical Image Comparison of Rock Ejecta Blanket. a, High-resolution optical image from ShadowCam, with a resolution of 1.7 m/pixel. The location of the rock ejecta blanket is at coordinates (82.58°S, 149.25°E). b, SAR image of the same area, with a resolution of 7.5 m/pixel. This image clearly displays the morphology of the rock ejecta blanket. c, Generated high-resolution optical image with a resolution of 1.9 m/pixel.

The ejecta blanket surrounding a crater can be used to determine the degree of degradation of craters[16]. It can be seen in Fig. 5c that the crater in the white solid box has a bright ejecta blanket, which means the crater is a fresh crater. Meanwhile, the crater within the white box in Fig. 5f is a moderately degraded crater, which does not have an ejecta blanket but contains rough rocks inside the crater. Fig. 6a shows a high-resolution optical image from ShadowCam, where rocks are invisible. Figs. 6b and c are the SAR image and generated high-resolution optical image. The ejecta blankets are bright in Figs. 6b and c, indicating the relatively young age[16]. The length and direction of the ejecta blanket in SAR images can be used to infer the impact direction and angle of the meteorite[17-19].

To validate the accuracy of the rocky ejecta blanket in the generated optical images, this study conducted simulations using optical and SAR methods. The specific simulation methods and results can be found in the IV. Discussion.

Lava tubes record the history of lunar volcanic geology. There are few studies about the lava tubes in PSR. Fig. 7a is a high-resolution optical image of the lava tube in PSR of Slater Crater from ShadowCam. The position of the lava tube is at (88.06°S, 112.65°E). The color of Fig. 7a is dark due to the large incidence angles of the scattered light. In Figs. 7b and c are the SAR image and the generated optical image. In Fig. 7c, the generated high-resolution optical image accurately reconstructs craters, rocks, and textures.

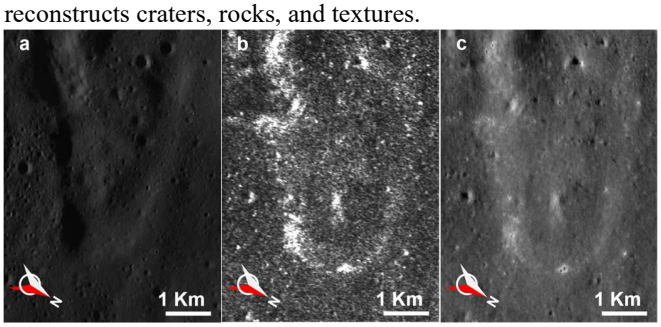

Fig. 7. Images of Lava Tubes. a, High-resolution optical image from ShadowCam with a resolution of 1.7 m/pixel. The position of the lava tube is at (88. 06°S, 112.65°E). b, SAR image of the same area, with a resolution of 7.5 m/pixel, clearly displaying the morphology of the lava tube. c, Generated high-resolution optical image with a resolution of 1.9 m/pixel.

The presence of lava tubes in the PSR indicates past volcanic activity. Lava tubes are typically found near volcanic vents, suggesting that the PSR may contain abundant volatile chemicals such as sulfur, iron, and oxygen, as well as volcanic debris that can be used as construction material[20, 21]. Due to their enclosed nature and limited exposure to the space environment, lava tubes may also serve as storage sites for water and other sediments. Therefore, searching for lava tubes within the PSR holds significant scientific importance.

IV. Discussion

A) Simulation of Optical images with different illumination angles

The study uses GAN networks to generate optical images from SAR images, preserving the sensitivity of SAR images to rocks and allowing observation of rock distribution. The style of the generated optical images is consistent with that of low-latitude optical images at small illumination angles. In addition, the distribution of rocks can be observed on the small illumination angles, and can not on the large illumination angles. This is verified through simulation. The intensity reflected from lunar surface is written as[2]:

$$I = \frac{TSI \times S_0 \times \cos(\theta_i) \times A \times G(\theta_i, \theta_e)}{\cos(\theta_t)} \quad (1)$$

Where TSI is the total solar irradiance, which is constant here and is ignored in the following calculations. A is albedo data from KAKUYA data, with a wavelength of 414 nm and an incident angle of 15.37°. $G(\theta_i, \theta_e)$ is the direction function of the reflection. θ_i is the solar incidence angle, θ_e is the angel between the line of the viewer and the normal, and θ_t is the angle of the slope, which can be seen in Fig. 8. $\cos(\theta_i)$ is used to model the solar irradiance on each slope while $\cos(\theta_t)$ is used to calculate the area of the tilted slope. The area of each slope $S_i = \frac{S_0}{\cos(\theta_t)}$, where the area S_0 of each slope projected on the horizontal plane is constant. The constant S_0 is ignored in calculation.

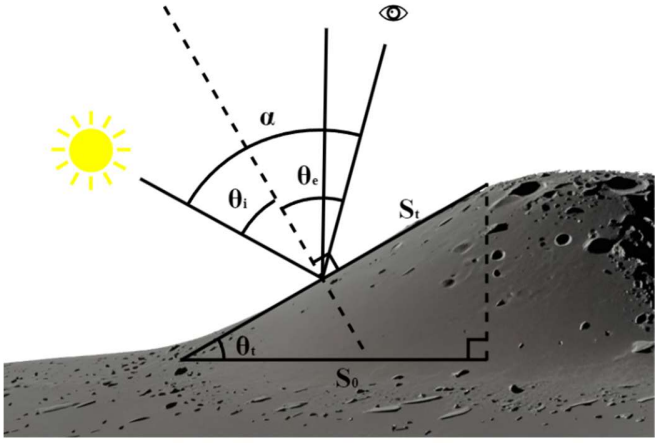

Fig. 8. Conceptual illustration. The relationship between the sun, the lunar surface, and the viewer.

The Lunar-Lambert model is used in simulation[22]:

$$G(\theta_i, \theta_e) = (1-\omega)\cos(\theta_i) + 2\omega \times \frac{\cos(\theta_i)}{\cos(\theta_i) + \cos(\theta_e)} \quad (2)$$

Which ω is a function of the phase angle α (i.e., the angle between the sunlight and the line of the viewer)[23]:

$$\omega = 1 - 0.019\alpha + 0.242 \times 10^{-3}\alpha^2 - 1.46 \times 10^{-6}\alpha^3 \quad (3)$$

This study selects a region at (8.74°N, 33.19°E) for simulation. KAKUYA data (MIA_3C5_03_02326N089E0334SC) with a resolution of 14.8 m/pixel of this area are used as the albedo A in Equation 1. DTM data (NAC_DTM_TRANQPIT1_E084N0332) with a resolution of 2 m/pixel are used for modeling the 3D morphology. The viewer observes the lunar surface at nadir point in the simulation.

Optical images under different solar illumination angles are simulated, as shown in Fig. 9. Figs. 9a-c are actual NAC optical images (M188021351, M1236388169, M1218738444) with a resolution of 1 m/pixel, and incident angles of 16.7°, 41.67°, and 69.68°, respectively.

In Figs. 9a and b, the rock eject blankets are bright in the surrounding lunar regolith. In Fig. 9c, the optical image cannot distinguish between rock and lunar regolith. The generated optical images are shown in Figs. 9d-f. The optical simulation images are consistent with the actual optical image, validating the reliability of the simulation results.

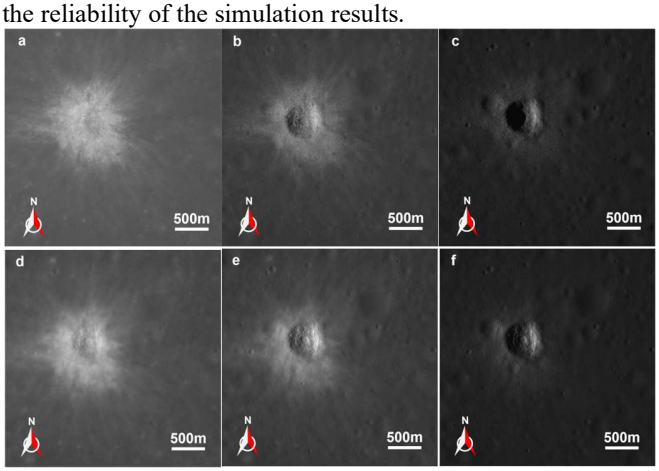

Fig. 9. Optical images from NAC and the corresponding simulation. a-c, The high-resolution NAC optical images (M188021351, M1236388169, M1218738444) with a resolution of 1.00 m/pixel, centered at the coordinates of the crater (8.74°N, 33.19°E). The illumination angles for Figs. 5a-c are 16.7°, 41.67°, and 69.68°. d-f, The simulated illumination images generated from the Lunar-Lambert model.

After impact events (such as meteorite impacts and volcanic eruptions), a large number of glass spheres (meteorite glass and volcanic glass) and rock fragments are generated, which have high specular reflection coefficients[24]. From KAGUYA data, the albedo A of rock is larger than the neighboring lunar regolith. To further explain the differences in intensity I between rocks and lunar regolith at different illumination angles, Fig. 10 shows the relationship between the image intensity I of rocks and lunar regolith as a function of solar incident angle.

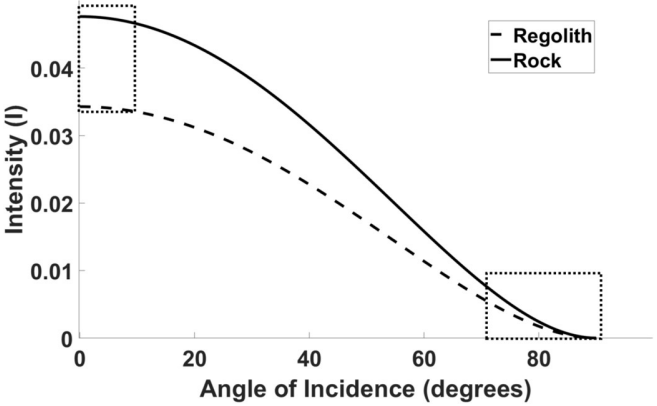

Fig. 10. A curve graph showing the variation of image intensity with incident angle. The curves illustrate the relationship between the image intensity of lunar regolith and rock as a function of solar incident angle.

By setting a threshold on KAKUYA data, the average albedo of rock for rocky areas is set to be 0.034 and the average albedo of lunar regolith for regolith is set to be 0.048. Here, it is assumed that $\theta_i = 0$. The variation of I for rocks and lunar regolith with solar incident angle is calculated.

In Fig. 10, at small illumination angles, there is $\cos(\theta_i)\approx 1$, $G(\theta_i,\theta_e)\approx 1$, and $I\approx A$. The intensity I of rocks is greater than that of lunar regolith by 0.013. As the solar incident angle increases, the image intensities I of lunar regolith and rocks decreases. At large incident angles from 70° to 90°, the difference in intensity I between rocks and lunar regolith is less than 0.002. Consequently, at large incident angles, the distribution of rocks is difficult to identify.

B) Simulation of SAR image

Different from optical cameras, SAR is sensitive to rock and topographical variations. In order to understand SAR images, SAR images with or without rocks are simulated, and compared with measured data for verification.

Fig. 11a shows the SAR image of the fresh crater in Fig. 9, where distinct rock ejecta blanket can be observed. The red mask in Fig. 11b is the ejecta blanket extracted from the SAR image, overlaid on the NAC optical image at a small illumination angle. It can be seen that the rock ejecta blanket in the SAR image is consistent with that in the optical image. Fig. 11c is the slope angle map of this area. Figs. 11d-f are enlarged images of the red box, which present the distribution of surface rocks.

In the simulation, the 3D morphology is constructed by DTM. The lunar topography is divided into small triangular meshes. The vertices of these triangles are defined by neighboring points from the DEM data. The raw data is simulated by KA-SPM dual-scale model, and the imaging is performed by Range-Doppler algorithm[25]. The components S_{pq}^n of the scattering matrix for mesh n depend on the area and reflectivity of that mesh. Therefore, S_{pq}^n can be expressed as[26]:

$$S_{pq}^n = \gamma_{pq}^n \sqrt{\frac{A_n}{4\pi}} \tag{4}$$

where γ_{pq}^n is the reflectivity from the mesh n. A_n is the area of the mesh n. The subscript q is the transmitted polarization and p is the received polarization. γ_{pq} is simulated by KA-SPM dual-scale model[27].

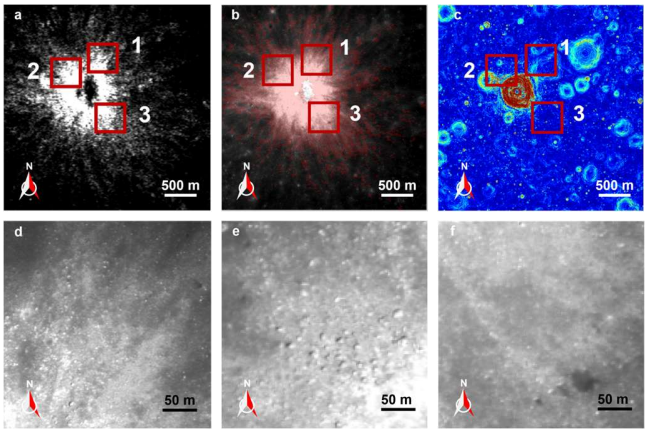

Fig. 11. Qualitative analysis of rock ejecta blanket in SAR and optical images. a-c, The rock ejecta blanket of fresh crater in the SAR, optical image, and slope angle map, respectively. The red mask indicates the rock ejecta blanket from SAR, which is consistent with the optical image. d-f, A high-resolution optical image displays three different rock distributions: in red box 1, there are clear boundaries of the rock distribution; in red box 2, a larger and denser rock distribution; and in red box 3, a sparse rock distribution.

In SAR simulation, the raw signals can be written as[28]:

$$h_{pq}(t,T) = \sum S_{pq}^n s^n(t,T) \tag{5}$$

Where a chirp modulation pulse is transmitted. There is

$$s^n(t,T) = \Pi\left[\frac{t-2R^n/c}{\tau/2}\right]\Pi\left[\frac{vT-x^n}{L_s/2}\right]\exp\left\{-i4\pi\frac{R^n}{\lambda}+i\pi K_r(t-\frac{2R^n}{c})^2\right\}n \tag{6}$$

$$\Pi(t) = \begin{cases} 1 & |t|\le 1 \\ 0 & |t|>1 \end{cases} \tag{7}$$

Here τ represents the pulse width, t is the time, v is the speed of the satellite, T is the azimuth time, x^n is the azimuth coordinate of the mesh n, R^n is the distance between the antenna and the mesh n, c is the speed of light in vacuum, λ is the wavelength, K_r is the chirp rate, $L_s = \lambda R / L_A$ is the real antenna azimuth footprint. The Range-Doppler algorithm is used to generate SAR images.

Figs. 12a and b show the simulated SAR image with and without rocks. The resolution of the simulated SAR images is 15 m/pixel. The DTM slope map in Fig. 11c cannot capture rock information. Therefore, a rough surface with $L = 15m$ and $\delta = 2m$ is overlaid in the rock ejecta blanket of the DTM to model the rocky surface. The rocky surface alters the radar incidence angle. The backscattering from patches with small incidence angles is significantly enhanced, resulting in a stronger overall echo from the rocky area.

Additionally, some small craters cannot be observed in SAR images because of the lower resolution of these images.

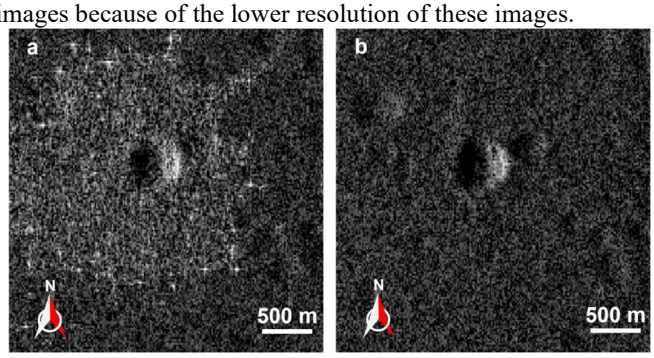

Fig. 12. Simulation Results. a, SAR image with rocks, showing distinct rock ejecta blanket. b, SAR image without rocks, lacking any rock ejecta blanket.

V. Conclusion

In this paper, SAR images in PSR are converted into high-resolution optical images with resolution of 1.9 m/pixel by CycleGAN and RealSRGAN. SSR and rocks that are invisible in ShadowCam images can be observed in the generated optical images. The generated images can be used to judge the degree of degradation of small craters in PSR and search for the lava tubes, which are the evidence of volcanic activity in PSR. The generated optical images are also helpful in analyzing the morphology of SSR and preparing the in-situ exploration missions.

ACKNOWLEDGMENT

The Mini-RF, ShadowCam, lunar orbiter laser altimeter (LOLA), and lunar reconnaissance orbiter camera (LROC) data used in this study are publicly available from http://pds-geosciences.wustl.edu, and https://ode.rsl.wustl.edu/moon/mapsearch. The RealSRGAN and CycleGAN network used in this study are also publicly available from https://github.com/xinntao/Real-ESRGAN and https://github.com/junyanz/pytorch-CycleGAN-and-pix2pix/.

REFERENCES

[1] D. A. Paige, M. A. Siegler, J. A. Zhang *et al.*, "Diviner Lunar Radiometer Observations of Cold Traps in the Moon's South Polar Region," *Science,* vol. 330, no. 6003, pp. 479-482, 2010/10/22, 2010.

[2] Z. Yin, N. Liu, and Y.-Q. Jin, "Simulation of the temperatures in the permanently shadowed region of the Moon's south pole and data validation," *Icarus,* vol. 411, pp. 115917, 2024/03/15/, 2024.

[3] V. T. Bickel, B. Moseley, I. Lopez-Francos *et al.*, "Peering into lunar permanently shadowed regions with deep learning," *Nature Communications,* vol. 12, no. 1, pp. 5607, 2021/09/23, 2021.

[4] M. S. Robinson, S. M. Brylow, M. Tschimmel *et al.*, "Lunar Reconnaissance Orbiter Camera (LROC) Instrument Overview," *Space Science Reviews,* vol. 150, no. 1, pp. 81-124, 2010/01/01, 2010.

[5] M. S. Robinson, S. M. Brylow, M. A. Caplinger *et al.*, "ShadowCam Instrument and Investigation Overview," *Journal of Astronomy and Space Sciences,* vol. 40, no. 4, pp. 149-171, 2023.

[6] C. I. Fassett, M. S. Robinson, G. W. Patterson *et al.*, "The LCROSS Impact Crater as Seen by ShadowCam and Mini-RF: Size, Context, and Excavation of Copernican Volatiles," *Geophysical Research Letters,* vol. 51, no. 18, pp. e2024GL110355, 2024/09/28, 2024.

[7] S. Nozette, P. Spudis, B. Bussey *et al.*, "The Lunar Reconnaissance Orbiter Miniature Radio Frequency (Mini-RF) Technology Demonstration," *Space Science Reviews,* vol. 150, no. 1, pp. 285-302, 2010/01/01, 2010.

[8] J. D. Hofgartner, and K. P. Hand, "A continuum of icy satellites' radar properties explained by the coherent backscatter effect," *Nature Astronomy,* vol. 7, no. 5, pp. 534-540, 2023/05/01, 2023.

[9] J. T. S. Cahill, B. J. Thomson, G. W. Patterson *et al.*, "The Miniature Radio Frequency instrument's (Mini-RF) global observations of Earth's Moon," *Icarus,* vol. 243, pp. 173-190, 2014/11/15/, 2014.

[10] L. Carrer, R. Pozzobon, F. Sauro *et al.*, "Radar evidence of an accessible cave conduit on the Moon below the Mare Tranquillitatis pit," *Nature Astronomy,* vol. 8, no. 9, pp. 1119-1126, 2024/09/01, 2024.

[11] D. B. Campbell, B. A. Campbell, L. M. Carter *et al.*, "No evidence for thick deposits of ice at the lunar south pole," *Nature,* vol. 443, no. 7113, pp. 835-837, 2006/10/01, 2006.

[12] S. Fu, F. Xu, and Y.-Q. Jin, "Reciprocal translation between SAR and optical remote sensing images with cascaded-residual adversarial networks," *Science China Information Sciences,* vol. 64, no. 2, pp. 122301, 2021/01/21, 2021.

[13] C. Ledig, L. Theis, F. Huszár *et al.*, "Photo-Realistic Single Image Super-Resolution Using a Generative Adversarial Network." pp. 105-114.

[14] J. Y. Zhu, T. Park, P. Isola *et al.*, "Unpaired Image-to-Image Translation Using Cycle-Consistent Adversarial Networks." pp. 2242-2251.

[15] P. Isola, J. Y. Zhu, T. Zhou *et al.*, "Image-to-Image Translation with Conditional Adversarial Networks." pp. 5967-5976.

[16] W. Fa, and V. R. Eke, "Unravelling the Mystery of Lunar Anomalous Craters Using Radar and Infrared Observations," *Journal of Geophysical Research: Planets,* vol. 123, no. 8, pp. 2119-2137, 2018/08/01, 2018.

[17] V. J. Bray, G. S. Collins, J. V. Morgan *et al.*, "The effect of target properties on crater morphology: Comparison of central peak craters on the Moon and Ganymede," *Meteoritics & Planetary Science,* vol. 43, no. 12, pp. 1979-1992, 2008/12/01, 2008.

[18] R. R. Herrick, and N. K. Forsberg-Taylor, "The shape and appearance of craters formed by oblique impact on the Moon and Venus," *Meteoritics & Planetary Science,* vol. 38, no. 11, pp. 1551-1578, 2003/11/01, 2003.

[19] V. Kaydash, Y. Shkuratov, and G. Videen, "Dark halos and rays of young lunar craters: A new insight into interpretation," *Icarus,* vol. 231, pp. 22-33, 2014/03/01/, 2014.

[20] D. M. Blair, L. Chappaz, R. Sood *et al.*, "The structural stability of lunar lava tubes," *Icarus,* vol. 282, pp. 47-55, 2017/01/15/, 2017.

[21] L. Xiao, P. Zhu, G. Fang *et al.*, "A young multilayered terrane of the northern Mare Imbrium revealed by Chang'E-3 mission," *Science,* vol. 347, no. 6227, pp. 1226-1229, 2015/03/13, 2015.

[22] A. S. McEwen, "Photometric functions for photoclinometry and other applications," *Icarus,* vol. 92, no. 2, pp. 298-311, 1991/08/01/, 1991.

[23] V. Lohse, C. Heipke, and R. L. Kirk, "Derivation of planetary topography using multi-image shape-from-shading," *Planetary and Space Science,* vol. 54, no. 7, pp. 661-674, 2006/07/01/, 2006.

[24] B.-W. Wang, Q. W. L. Zhang, Y. Chen *et al.*, "Returned samples indicate volcanism on the Moon 120 million years ago," *Science,* vol. 385, no. 6713, pp. 1077-1080, 2024/09/06, 2024.

[25] N. Liu, and Y. Q. Jin, "Pol-SAR Image Simulation of the Lunar Surface With Data Analysis of Chandrayaan-2 and Mini-RF," *IEEE Journal of Selected Topics in Applied Earth Observations and Remote Sensing,* vol. 16, pp. 10301-10310, 2023.

[26] F. Ulaby, D. Long, W. Blackwell *et al.*, *Microwave Radar and Radiometric Remote Sensing*, 2014.

[27] N. Liu, and Y. Q. Jin, "Simulation of Pol-SAR Imaging and Data Analysis of Mini-RF Observation From the Lunar Surface," *IEEE Transactions on Geoscience and Remote Sensing,* vol. 60, pp. 1-11, 2022.

[28] M. Shimada, "Imaging from Spaceborne and Airborne SARs, Calibration, and Applications," *Journal of The Remote Sensing Society of Japan,* vol. 39, no. 4, pp. 323-323, 2019.

Tong Xia was born in Shandong, China, in 1997. He received the B.E. degree in electronic information engineering from Shanghai Normal University in 2022. He is currently working toward the M.S. degree in electronic information at the Key Laboratory for Information Science of Electromagnetic Waves (MoE) for Advanced Study, School of Information Science and Technology, Fudan University, Shanghai, China. His research interests include AI for Science, deep space exploration, and microwave planetary remote sensing.

Niutao Liu was born in Jiangsu, China, in 1994. He received the B.S. degree in telecommunication engineering from the Nangjing University of Posts and Telecommunications, Nanjing, China in 2016. He received the Ph.D. degree in electromagnetic field and microwave technology from Fudan University, Shanghai, China in 2021. Now, he is an Assistant Professor with the Key Laboratory for Information Science of Electromagnetic Waves (MoE), Fudan University. His research interests include microwave planetary remote sensing, infrared remote sensing, computational electromagnetics, and synthetic aperture radar data analysis.

Zheng Yi received the B.E degree in electronic information science and technology from Northwest University, Xi'an, China. He is currently pursuing the M.S. degree in artificial intelligence with the Key Laboratory for Information Science of Electromagnetic Waves (MoE), Fudan University, Shanghai, China.His current research interests include deep learning and image processing.

Ya-Qiu Jin (SM'89, F'0**4, LF18)** graduated from Peking University, Beijing, China in Atmospheric Physics, 1970, and received the M.S., E.E., and Ph.D. degrees from the Massachusetts Institute of Technology, Cambridge, USA in 1982, 1983 and 1985, respectively. All these degrees were from Electrical Engineering and Computer Science. He was the Research Scientist of AER (Atmospheric Environmental Research, Inc., Cambridge) in 1985, Research Associate Fellow of City University of New York in 1986-1987, and Visiting Professor in University of York, UK in 1993 sponsored by the UK Royal Society. He was also awarded by the Senior Research Associateship in NOAA/NESDIS by USA National Research Council, 1996. He is currently the Te-Pin Professor, and Director of Key laboratory for Information Science of Electromagnetic Waves (MoE), and Institute of EM Big data and Intelligence Remote Sensing, Fudan University, Shanghai, China.

Dr. Jin is the Academician of CAS (Chinese Academy of Sciences), and the Life Fellow of IEEE, Fellow of TWAS (the World Academy of Sciences for Advances of Developing World), and IAA (International Academy of Astronautics). He was one of the first group of the IEEE GRSS Distinguished Speakers. He was co-Chair of TPC for IGARSS2011 in Vancouver Canada, and Co-General Chair for IGARSS2016 in Beijing, China. He was the Associate Editor of IEEE Transactions on Geoscience and Remote Sensing (2005-2012), and IEEE ACCESS (2016-18), the member of IEEE GRSS AdCom and Chair for IEEE Fellow Evaluation of GRSS (2009-2011). He is now the Member of IEEE GRSS Major Awards Committee.

His main research interests include electromagnetic scattering and radiative transfer in complex natural media, microwave satellite-borne remote sensing, as well as theoretical modeling, information retrieval and applications in earth terrain and planetary surfaces, and computational electromagnetics.

He has published more than 850 papers in refereed journals and conference proceedings and 17 books, including *Polarimetric Scattering and SAR Information Retrieval* (Wiley and IEEE, 2013), *Theory and Approach of Information Retrievals from Electromagnetic Scattering and Remote Sensing* (Springer, 2005), *Electromagnetic Scattering Modelling for Quantitative Remote Sensing* (World Scientific, 1994),

He received IEEE GRSS Distinguished Achievement Award (2015), Golden Florin Award (2022), IEEE GRSS Education Award (2010), the China National Science Prize (2011, 1993), the Shanghai Sci/Tech Gong-Cheng Award (2015), the first-grade MoE Science Prizes (1992, 1996 and 2009) among many other prizes.

Feng Xu (Senior Member, IEEE) received the B.E. degree (Hons.) in information engineering from Southeast University, Nanjing, China, in 2003, and the Ph.D. degree (Hons.) in electronic engineering from Fudan University, Shanghai, China, in 2008.

From 2008 to 2010, he was a Post-Doctoral Fellow with the National Oceanic and Atmospheric Administration (NOAA) Center for Satellite Applications and Research, Camp Springs, MD, USA. From 2010 to 2013, he worked with Intelligent Automation Inc., Rockville, MD, USA, and the NASA Goddard Space Flight Center, Greenbelt, MD, USA, as a Research Scientist. He was selected for China's Global Experts Recruitment Program in 2012 and subsequently returned to Fudan University in 2013, where he is currently a Professor and the Vice Dean of the School of Information Science and Technology and the Director of the MoE Key Laboratory for Information Science of Electromagnetic Waves. His research interests include electromagnetic scattering modeling, synthetic aperture radar (SAR) information retrieval, and radar system development.

Dr. Xu was a recipient of the Second-Class National Nature Science Award of China in 2011, the 2014 Early Career Award of the IEEE Geoscience and Remote Sensing Society, and the 2007 SUMMA Graduate Fellowship in the advanced electromagnetics area. He is the Founding Chair of the IEEE GRSS Shanghai Chapter. He was an Associate Editor for the IEEE GEOSCIENCE AND REMOTE SENSING LETTERS.